Hindawi
Shock and Vibration
Volume 2020, Article ID 2905341, 10 pages
https://doi.org/10.1155/2020/2905341

Research Article

Simulation of the Vibratory Behavior of Slender Shafts Subject to Transverse Loads Moving in the Axial Direction

F. Bucchi and P. Forte

Department of Civil and Industrial Engineering, University of Pisa, 56122 Pisa, Largo Lazzarino, Italy

Correspondence should be addressed to F. Bucchi; francesco.bucchi@unipi.it

Received 30 April 2019; Revised 7 November 2019; Accepted 29 November 2019; Published 3 January 2020

Academic Editor: Stefano Marchesiello

In various machines of the manufacturing industry, and in particular in paper converting machinery, there are shafts operating under conditions similar to that of a slender beam subjected to a transverse load moving in the axial direction. This condition can lead to vibrations and consequent deterioration of the machine performance and of the product quality. The problem has been theoretically studied in the literature since the 1990s. While shaft mass and stiffness are universally considered among the most influential parameters on its vibratory behavior, less obvious and not investigated in the literature is the influence of the spatial interval between two successive loads, an aspect that should be considered in the shaft design phase. In fact, if that is less than the length of the shaft, i.e., if there is more than one transverse load on the shaft at a given time, the vibration level may decrease with respect to the single-load configuration. This work describes the development of a mathematical model of a slender shaft hinged at its ends, representing the rotor of a paper roll perforating unit, with the SW Mathematica. The effect of a load moving axially at a given speed followed by similar loads after given spatial intervals was simulated investigating the influence of speed and load interval on shaft vibrations and resonance. The results showed how reducing the load interval can lead to a reduction of the shaft vibration which is a useful indication on possible design corrective actions.

1. Introduction

The problem of vibrations of structures due to moving loads is of interest in various engineering fields as overviewed in [1]. Beams subjected to moving loads have been dealt with especially in bridge design, and quite several papers can be found in the literature on the topic, among which stands out Frýba's overview [2]. Quite fewer papers have addressed similar topics in the field of mechanical engineering that is vibrations of shafts subjected to moving loads due, for example, to cutting tools. The first treatise [3] compares different beam models. The Euler–Bernoulli beam, a Rayleigh beam (which includes rotary inertia effects), and a Timoshenko beam (which includes rotary inertia and shear deformation effects) are used to model the rotating shaft. The first appears suitable for slender shafts and the others for stiffer ones. In [4], the effect of the shaft rotational speed is investigated, finding that an increase of it has minimal effect on the deflection in the direction of the applied load, while the deflection in the orthogonal direction of the applied load increases steadily with increased rotational speed. In [5, 6], the influence of moving load deflection dependence is studied and it is observed that if the load is not deflection dependent, the resonance condition is simply given by the equality of load frequency and beam natural frequency, while the deflection dependence tends to reduce the values of the beam displacement component in the loading direction. Moreover, the deflection-dependent loading produces time-dependent coefficients in the governing equations and the possibility of parametric resonance and instability when time dependence is periodic. The vibration in the lathing process has been specifically investigated considering a moving transverse force in [7] and a more realistic three-directional force on the rotating workpiece modelled as a

Rayleigh or Timoshenko beam in [8–10], assuming the clamped-hinged supports and including as in [11] the effect of support elasticity.

Starting from this background, this article presents a mathematical model for slender shafts subject to moving transverse loads to ideally simulate the industrial perforation process of paper rolls. The rotor of a paper roll perforating unit is a slender shaft with a given number of helicoidal blades that come into contact with a countershaft to perforate the paper sheet. Due to the helical shape of the blades, the contact is ideally a point that moves axially as the shaft rotates. There can be more than one blade simultaneously in contact with the counteracting rotor depending on the number of blades and on the helix angle. The modelling and simulation of the dynamic behavior of such a system is of interest for the designer in order to avoid vibrations and consequent deterioration of the machine performance and of the product quality. The influence of various parameters including speed and load interval on shaft vibrations and resonance was investigated.

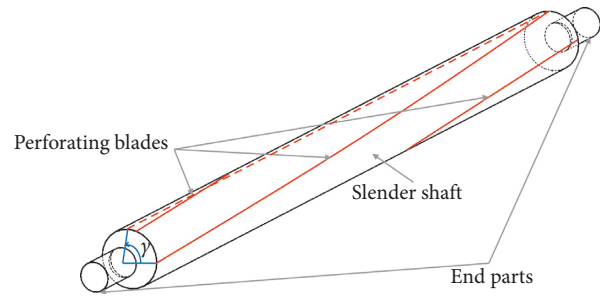

Figure 1: Geometry of the analyzed shaft.

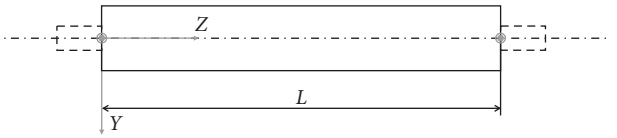

Figure 2: Shaft model.

2. Slender Shaft Model

2.1. Slender Shaft Geometry. The shaft geometry considered in this analysis is shown in Figure 1. The end parts have length L_0 and a lower diameter in order to fit radial bearings.

The central part of the shaft is assumed to have uniform cross section of diameter D and length L. Along this part, a given number n_b of longitudinal blades are fixed to the rotor. The blades are adapted on the shaft following a helicoidal pattern for a progressive cut. The countershaft is installed parallel to the perforating shaft, and it is assumed to have the same geometry.

2.2. The Euler–Bernoulli Model. The model of Euler–Bernoulli is convenient for slender shafts such as in this case because, due to shaft slenderness, both shear and gyroscopic effects can be neglected and the shaft can be treated as a nonrotating beam. In [12], the gyroscopic effects for a spinning beam as function of the slenderness ratio are investigated showing that they decrease with it and are negligible for the first natural frequencies. The simplified Euler–Bernoulli model is recommended in [3] for subcritical rotational speed and Rayleigh beam coefficient, $\beta = (\pi/L)(\sqrt{I/A})$, lower than 0.15, as in the present case ($\beta = 0.05$).

The shaft, schematically represented in Figure 2, in this first analysis, is assumed of constant cross section, of length L, and directly hinged to the frame, neglecting the compliance and inertia of the end parts of reduced cross section, which are schematically represented using the dashed lines.

Taking a reference system XYZ having origin on the left end of the shaft, as indicated in Figure 2, and a longitudinal coordinate z, the dynamic equilibrium equation of the shaft can be written as

$$EI\frac{\partial^4 u(z,t)}{\partial z^4} + \rho A\frac{\partial^2 u(z,t)}{\partial t^2} = P(z,t), \tag{1}$$

where EI is the flexural stiffness of the shaft section, with E Young's modulus of the shaft material, I the moment of inertia of the shaft cross section about a transverse axis, ρA, ρ the shaft density, A the area of its cross section, u the transverse displacement parallel to Y, P the moving load, and z and t the space and time variables, respectively.

The boundary conditions are imposed at the shaft ends in order to model the hinge constraints:

$$u(0,t) = 0, \tag{2}$$

$$\frac{\partial^2 u(0,t)}{\partial z^2} = 0, \tag{3}$$

$$u(L,t) = 0, \tag{4}$$

$$\frac{\partial^2 u(L,t)}{\partial z^2} = 0. \tag{5}$$

Moreover, the following initial conditions are imposed:

$$u(z,0) = 0, \qquad \frac{\partial u(z,0)}{\partial z} = 0. \tag{6}$$

2.3. Contact Force Model. Due to the helicoidal shape of the blades, the contact patch where the perforation occurs moves longitudinally (along z). The blade pitch γ (defined as the angle measured on a plane perpendicular to the shaft axis, between the two ends of a blade), shown in Figure 1, is defined as

$$\gamma = \frac{2\pi c}{n_b}, \tag{7}$$

where n_b is the number of the blades and c is the contact ratio. If the blades are equally spaced and there is only one contact patch between the two shafts at any time, $c = 1$. On the contrary, if more than one contact patch exists during a portion of the shaft rotation $c > 1$, while if no contact occurs at some given time, $c < 1$.

Consequently, the load speed is computed as

$$v(c) = \frac{n_b \omega L}{2\pi c}, \tag{8}$$

where ω is the shaft angular speed and the load frequency f_P is related to the shaft angular speed and to the number of blades as follows:

$$f_P = \frac{n_b \omega}{2\pi}. \tag{9}$$

The load amplitude $P(z)$ at a given time was implemented, without introducing local contact models, as a Gaussian pressure distribution having mean value in z_0 and standard deviation σ:

$$P(z) = \frac{P_0}{\sqrt{2\pi}\sigma} e^{-\left((z-z_0)^2/2\sigma^2\right)}, \tag{10}$$

where P_0 is the amplitude of the distribution resultant force.

The load time dependence can then be expressed through the time-dependent position of z_0. If no less than one and no more than two contact patches exist at any time during the operation, that is, $1 \le c \le 2$, and the number of blades is even, it is useful to assume the moving load as the sum of two consecutive load trains (related to two consecutive blades), moving at constant speed $v(c)$ along the shaft, each one having period $2T_P$ and phase shift equal to T_P, with T_P the reciprocal of the previously defined load frequency:

$$P(z,t,c) = \frac{P_0}{\sqrt{2\pi}\sigma}\left(e^{-\left(\left(z-v(c)\widehat{t_1}\right)^2/2\sigma^2\right)} + e^{-\left(\left(z-v(c)\widehat{t_2}\right)^2/2\sigma^2\right)}\right), \tag{11}$$

where

$$\widehat{t_1}(t) = t - 2T_P\left\lfloor \frac{t}{2T_P} \right\rfloor,$$
$$\widehat{t_2}(t) = t - 2T_P\left(\left\lfloor \frac{t+T_P}{2T_P} \right\rfloor - \frac{1}{2}\right), \tag{12}$$

where $\lfloor - \rfloor$ is the symbol used for the floor function.

Figure 3 shows the contact force distribution as a function of space coordinate (z) and time (t), assuming $c = 1$, while Figure 4 shows the contact force distribution, at a given time, for three different loading ratios. It is easy to envisage that the larger the contact ratio is, the spatially closer the loading force distribution peaks are.

2.4. Mathematical Problem Solution. Equation (1) is a partial differential equation involving two variables, z and t. In order to make the equation an ordinary differential equation, modal superposition is employed as in [13, 14] and the solution is assumed as the product of two functions that depend only on the spatial and temporal coordinates, respectively, as follows:

$$u(z,t) = \sum \phi_n(z) q_n(t), \tag{13}$$

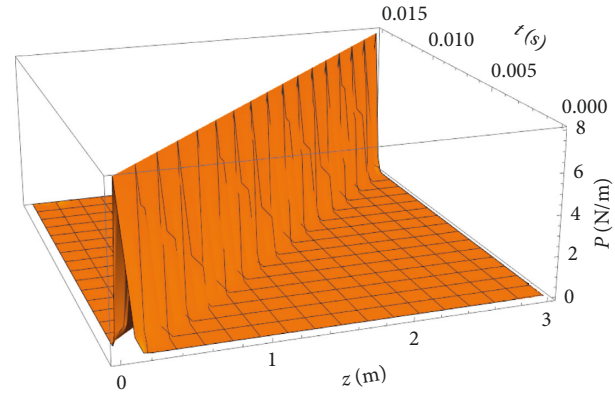

Figure 3: Contact force as a function of space and time for $c = 1$.

where $q(t)$ is the generalized coordinate and $\phi_n(z)$ is the shape of the nth vibration mode.

The shape function describing each mode is as follows:

$$\phi_n(z) = \sin\left(\frac{n\pi z}{L}\right), \tag{14}$$

and, for each nth vibration mode, substituting $u(z,t)$ and integrating with respect to the spatial coordinate the left- and right-hand parts of equation (1), we obtain

$$\frac{\rho A L}{2}\ddot{q}_n(t) + EI\frac{n^4\pi^4}{2L^3}q_n(t) = \int_0^L P(z,t)\sin\left(\frac{n\pi z}{L}\right)dz, \tag{15}$$

which is a time-dependent ordinary differential equation. The right-hand term of equation (15) is computed numerically to generalize the problem solution also for contact force models which cannot be integrated analytically.

Considering the homogeneous equation associated with equation (15) and the boundary conditions described by equations (2)–(5), the natural frequency associated to each vibration mode of the system is

$$f_n = \frac{\pi}{2}\left(\frac{n}{L}\right)^2\sqrt{\frac{EI}{\rho A}}. \tag{16}$$

2.5. Simulation and Results. The previous equations were implemented in a numerical, solver and the solution was found for different shaft angular speeds ω and different contact ratios c, considering the shaft parameters listed in Table 1. The results are here compared in terms of shaft transverse displacement at the center of the forcing patch.

Preliminary simulations were performed to assess the effect of standard deviation of the pressure distribution, considering the 0.05–0.20 m range, and no appreciable differences in the shaft deformation were found depending on this parameter.

In addition, the first natural frequency of the shaft was computed by equation (16) and resulted 44.6 Hz, which corresponds to a shaft critical speed of 2677 rpm, while the second natural frequency of 178.4 Hz corresponds to a shaft critical speed of 10706 rpm, well beyond the shaft speed

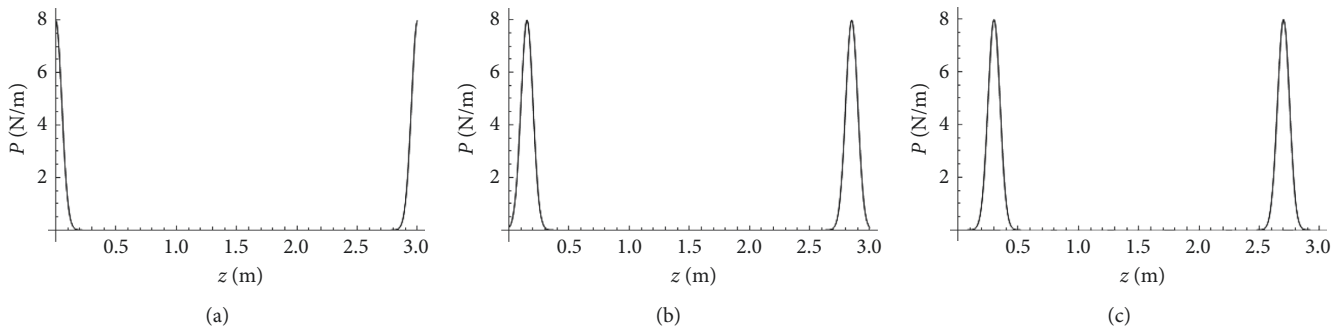

Figure 4: Contact force at a given time for three different contact ratios. (a) $c = 1$, (b) $c = 1.1$, and (c) $c = 1.25$.

Table 1: Shaft parameters used in the simulation.

Shaft length	L	3.0 m
Shaft diameter	D	0.2 m
Number of perforating blades	n_b	4/6
Shaft angular speed	ω	200–1200 rpm
Shaft flexural stiffness	EI	1.6×10^7 Nm^2
Shaft density	ρ	7800 kg/m^3
Shaft cross-sectional area	A	0.0314 m^2
Contact force intensity	P_0	1000 N
Contact ratio	c	1.0/1.1/1.25
Standard deviation of the pressure distribution	σ	0.1 m

operating range. Indeed, the considered speed range (200–1200 rpm) is under-critical, apparently well below the first critical speed. However, since the number of blades is equal to 4 or 6, the loading frequency f_p is greater than the shaft rotating frequency and can reach and exceed the first natural frequency of the shaft.

Three case studies are presented in this section to investigate the influence of the blade number, the rotational speed, and the contact ratio:

(i) Case Study 1: 4 blades, variable ω, $c = 1$

(ii) Case Study 2: 6 blades, variable ω, $c = 1$

(iii) Case Study 3: 4–6 blades, load-critical angular speed, $c = 1$

(iv) Case Study 4: 4 blades, variable ω, $c \neq 1$

The results and discussion may be presented separately, or in one combined section, and may optionally be divided into headed subsections.

2.5.1. Case Study 1. Figure 5 shows the normalized slender shaft deformation contribution related to the first vibration mode ($n = 1$ in equation (15)) for six load positions obtained considering the shaft rotating at $\omega = 400$ rpm. As occurs in static conditions, the shaft deforms under the effect of the constant amplitude contact force and the deformation becomes greater as the load approaches the central position of the shaft. Having considered only the first vibration mode, the maximum displacement occurs exactly at midspan.

Figure 6 is obtained considering the envelope of the shaft transverse displacement at the center of the pressure distribution. Since the shaft deformation, in general, is not the same for two or more consecutive load runs, Figure 6 shows the above described envelope considering 3 s as simulation time, which corresponds to 40–240 load runs depending on the considered shaft angular speed. Considering the maximum deformation of the shaft, it is obtained at 600 rpm, while remarkable values in negative shaft deformation are obtained at 800 rpm.

The load amplification and critical conditions are strictly related to the relation between the first natural frequency of the shaft and the load frequency. Indeed, considering the equality of f_P and f_1, the following expression of the load-critical angular speed $\overline{\omega}$ is obtained:

$$\overline{\omega} = \frac{2\pi c f_1}{n_b}. \tag{17}$$

If the 4-blade case is considered, the load critical angular speed is 669 rpm, that is, between 600 and 800 rpm case studies, where the maximum shaft deformation occurs. Therefore, the deformation amplification corresponding to these speed values can be ascribed to the proximity of the load-critical speed.

Considering that, in real operation, the contact load is not constant as assumed in the simulations but actually depends on elastic deformation, Figure 6 is very useful to give an idea of the load variation that would occur during the perforation process. Indeed, if the shaft displacement were almost constant at the forcing point (excluding the cases when the center of the pressure distribution is close to the ends of the shaft, where the rigid support assumption does not allow shaft deformation) when it moves along the shaft, as it happens for $\omega = 1000 - 1200$ rpm, the perforation would be uniform and regular. On the contrary, if the transversal displacement substantially varied with the load position, the perforation could be uncertain, as it happens for $\omega = 600$ rpm. In addition, if the shaft displacement was too high, separation could occur between the shafts and perforation be interrupted; on the contrary, if the displacement reached negative values, in real application, the perforating load would increase beyond the preload and blade failure or wear might occur. However, this effect will be investigated more in depth in future studies.

Another interesting parameter which can be analyzed in Figure 6 is the variation of the shaft deformation for different load runs. For low angular speed values (200–400 rpm), the

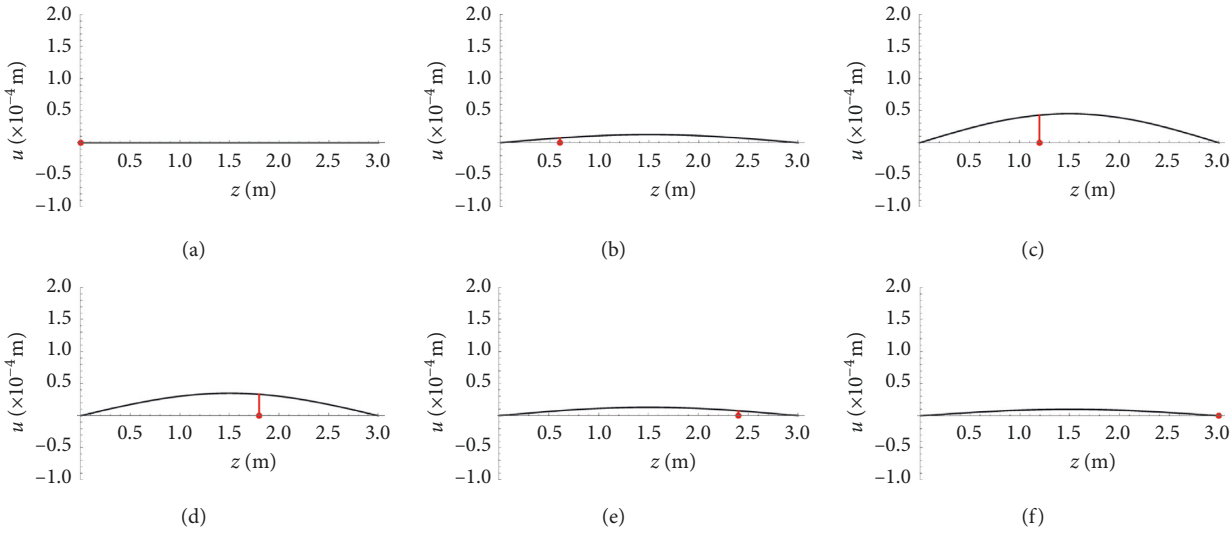

Figure 5: Shaft deformation for different load positions (the red point represents the center of the pressure distribution)—ω = 400 rpm.

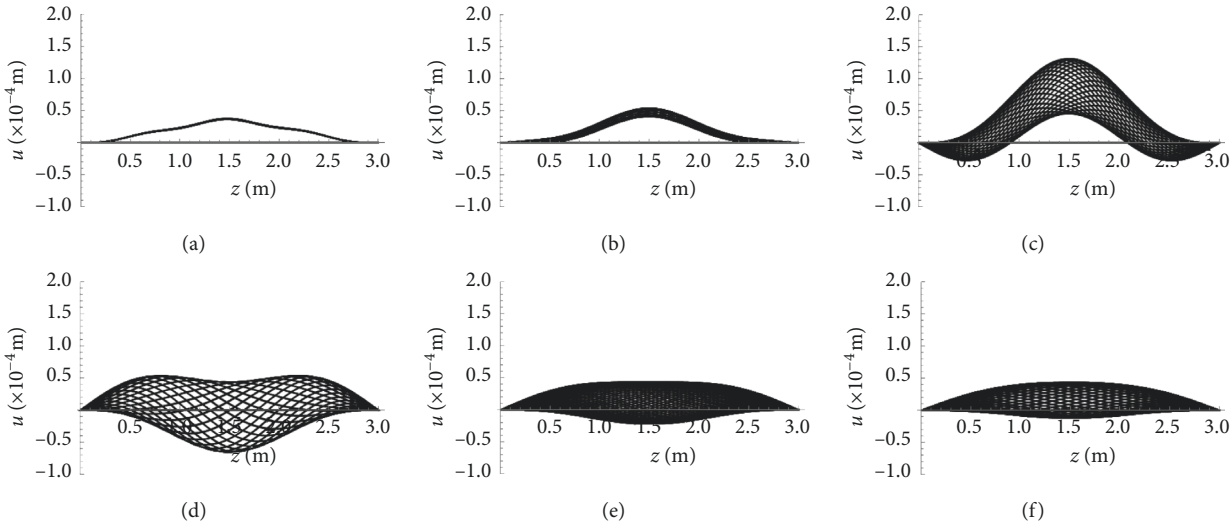

Figure 6: Shaft displacement at the forcing point during several loading periods for different angular speeds—first natural mode contribution, 4 blades. (a) ω = 200 rpm; (b) ω = 400 rpm; (c) ω = 600 rpm; (d) ω = 800 rpm; (e) ω = 1000 rpm; (f) ω = 1200 rpm.

curves related to the shaft deformation for different load runs are almost overlapped, proving that consecutive cycles produce almost identical shaft deformations. This can be explained considering that the loading frequency, which is 13.3 Hz at 200 rpm and 26.6 Hz at 400 rpm, is much lower than the first shaft natural frequency so that the amplification factor is close to 1 and the phase shift is close to zero. For higher rotational speeds and loading frequencies, there is a phase shift between the forcing function and the response so that when the force starts its run finds a different shaft deformation from the previous one and that creates a bundle of curves of the shaft displacement at the forcing point.

This phenomenon is more appreciable if the displacement versus time of a point belonging to the shaft is analyzed. In particular, Figure 7 shows the amplitude of the fast Fourier transform (FFT) of the central point of the shaft ($z = L/2$) for all the considered angular speeds. For each speed, a component appears at f = 44.6 Hz (indicated in Figure 7 by a gray arrow), which corresponds to the shaft critical frequency f_1. The amplitude of this component peak is greater for ω = 600 − 800 rpm, which, as discussed, are the shaft angular speed values closer to the load-critical speed. Furthermore, for each plot, one or more peaks appear for frequency values equal to the load frequency f_p or its multiples. Consequently, these load-frequency peaks are associated with higher frequencies as the shaft angular speed rises. Also in this case, the amplitude of the load-frequency peak is greater for ω = 600 − 800 rpm, again due to the proximity between load speed and load-critical speed.

Based on this analysis, it should be clear why the wider or narrower bundle of curves appear in Figure 6. Considering underload-critical speed values, ω = 200 − 400 rpm, the

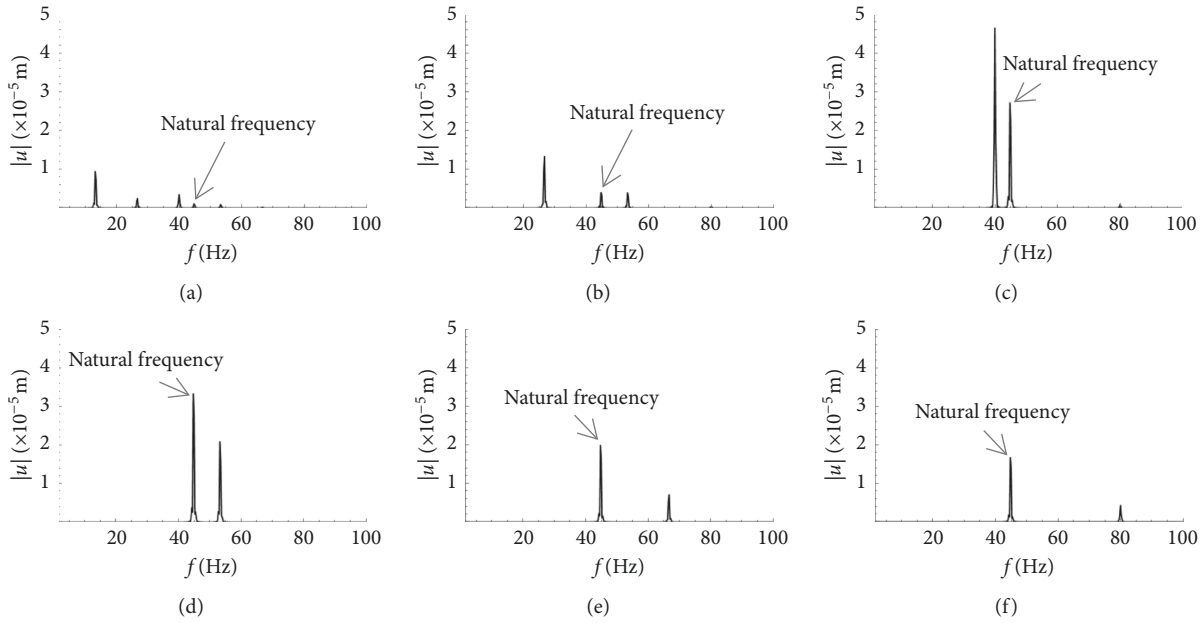

Figure 7: FFT of the shaft displacement at the forcing point during several loading periods for different angular speeds—4 blades. (a) $\omega = 200$ rpm; (b) $\omega = 400$ rpm; (c) $\omega = 600$ rpm; (d) $\omega = 800$ rpm; (e) $\omega = 1000$ rpm; (f) $\omega = 1200$ rpm.

bundle of curves appears narrow since the shaft response is dominated by the load-frequency component. Similarly, for overload-critical speed values, $\omega = 1000 - 1200$ rpm, the natural frequency component is predominant, even if a nonnegligible component at the load frequency exists and the bundle of curves appears slightly wider than for underload-critical speed. Finally, considering almost load-critical speed, $\omega = 600 - 800$ rpm, the natural frequency and the load frequency components have both significant amplitude in the shaft response and the bundle of curves appears wide.

In this case study, the contribution of the second vibration mode was also analyzed, solving equation (15) with $n = 2$. The results in terms of shaft displacement at the forcing point during several loading periods for different angular speeds are shown in Figure 8. The deformed shape is different if compared to the shape found for $n = 1$ because the shape functions ϕ_1 and ϕ_2 are different and the amplitude of the shaft deformation substantially decreases as the considered mode index rises. In particular, for $n = 2$, the maximum shaft deformation is less than 10% of the maximum shaft deformation found for $n = 1$. In addition, the maximum displacement for $n = 2$ slightly increases with the shaft speed but, since the operating range is well below the critical speed related to the second vibration mode, the displacement amplification in the considered range is not pronounced. These findings confirm what is well known [2] about the contribution of the first mode with respect to the others to the beam response, in particular as regards the maximal one, small load velocities and lightly damped beams [13, 15]. For this reason, the following analysis will be presented considering only the contribution of the first natural vibration mode without introducing appreciable errors in the results and without affecting the validity of the conclusions.

2.5.2. Case Study 2. Figure 9 shows the displacement of the shaft axis for several speeds considering the 6-blade case. In this case, the maximum displacement is found at 400 rpm and the reason can be understood considering again equation (16). In this case, the load-critical angular speed $\overline{\omega}$ is 446 rpm, and 400 rpm is the closest speed value among the considered ones. This result is again related to the shaft first natural frequency and resonance speeds.

At lower speed, i.e., 200 rpm, similarly to the 4-blade case, the curves are almost overlapped, while the magnification effect found at 400 rpm quickly vanishes, being the shaft response almost the same for speed values higher than 600 rpm.

2.5.3. Case Study 3. In order to assess the shaft deformation close to the load-critical angular speed $\overline{\omega}$ computed in equation (16), a simulation was performed for each blade configuration. In particular, the simulations were carried out at 0.98 $\overline{\omega}$ because the shaft has no damping and the exact load-critical angular speed could produce singular results.

Figure 10 shows the shaft deformation at 660 rpm and 440 rpm for the 4-blade and 6-blade configurations, respectively. It is worth noting that the vertical axis range is larger than the one considered in the previous plots, since the operation close to the load-critical angular speed produces larger deformation (about 0.7 mm for both blade configurations). No appreciable differences arise if 4-blade and 6-blade configurations are compared, being both results critical for the perforation operation. Indeed, in the real application a nonconstant perforation force, which would result particularly high when the deformation is negative (close to the shaft ends) and low, or eventually zero, in the central part of the shaft where detachment may occur, would cause a nonuniform perforation line.

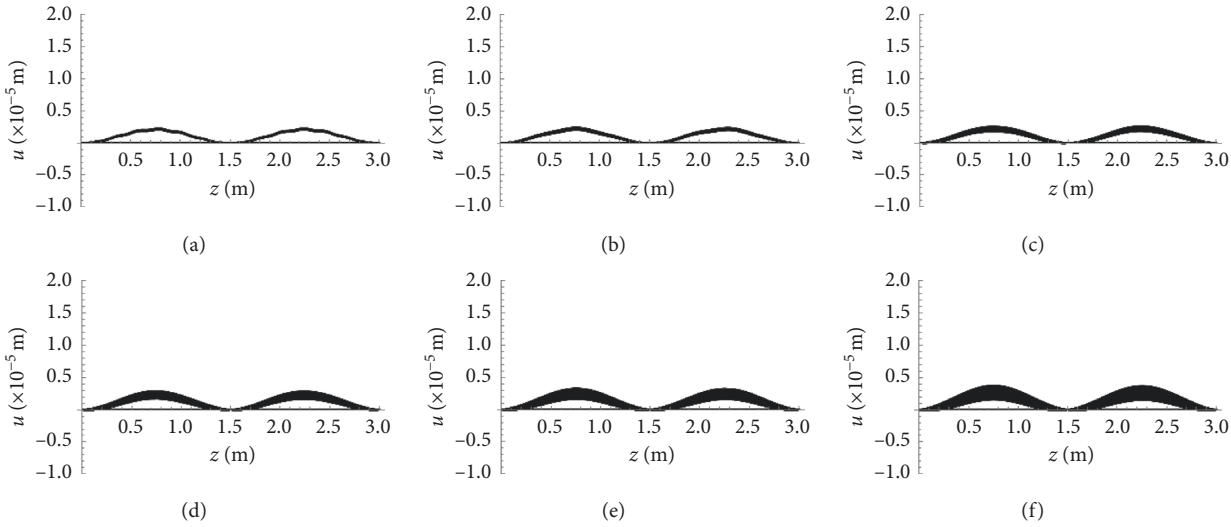

Figure 8: Shaft displacement at the forcing point during several loading periods for different angular speeds—second natural mode contribution, 4 blades. (a) ω = 200 rpm; (b) ω = 400 rpm; (c) ω = 600 rpm; (d) ω = 800 rpm; (e) ω = 1000 rpm; (f) ω = 1200 rpm.

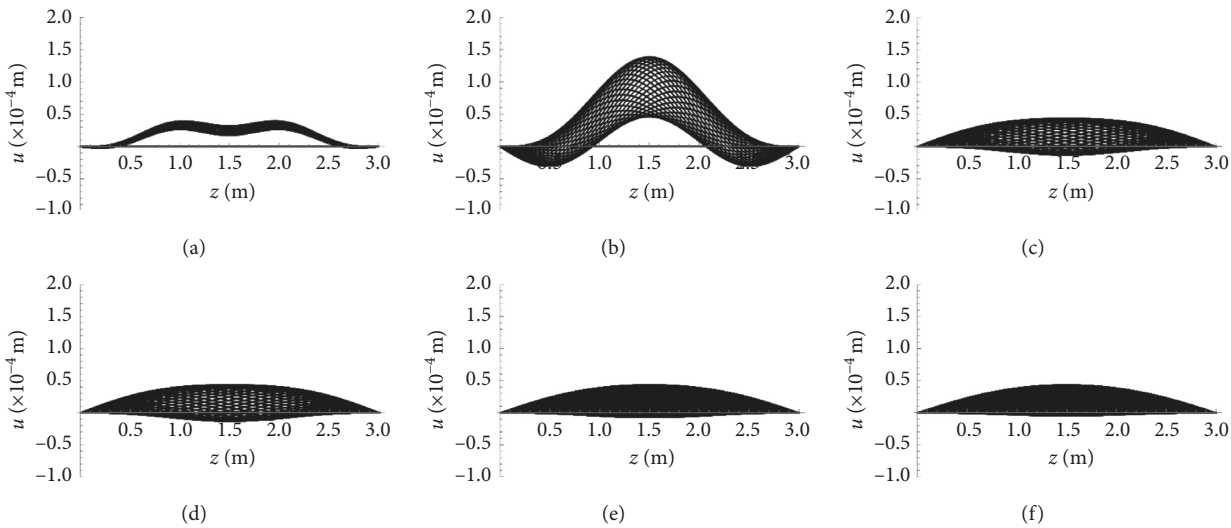

Figure 9: Shaft displacement at the forcing point during several loading periods for different angular speeds—6 blades. (a) ω = 200 rpm; (b) ω = 400 rpm; (c) ω = 600 rpm; (d) ω = 800 rpm; (e) ω = 1000 rpm; (f) ω = 1200 rpm.

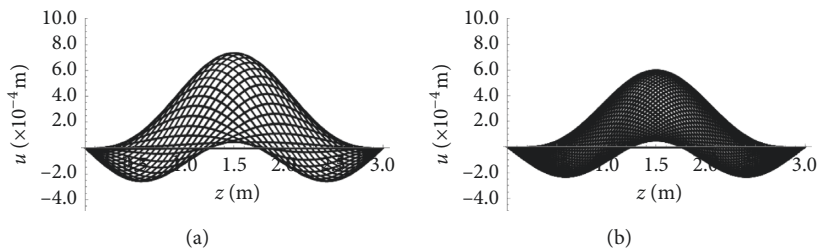

Figure 10: Shaft displacement at the forcing point during several loading periods for 98% of the load-critical angular speed for c=1. (a) 4 and (b) 6 blades.

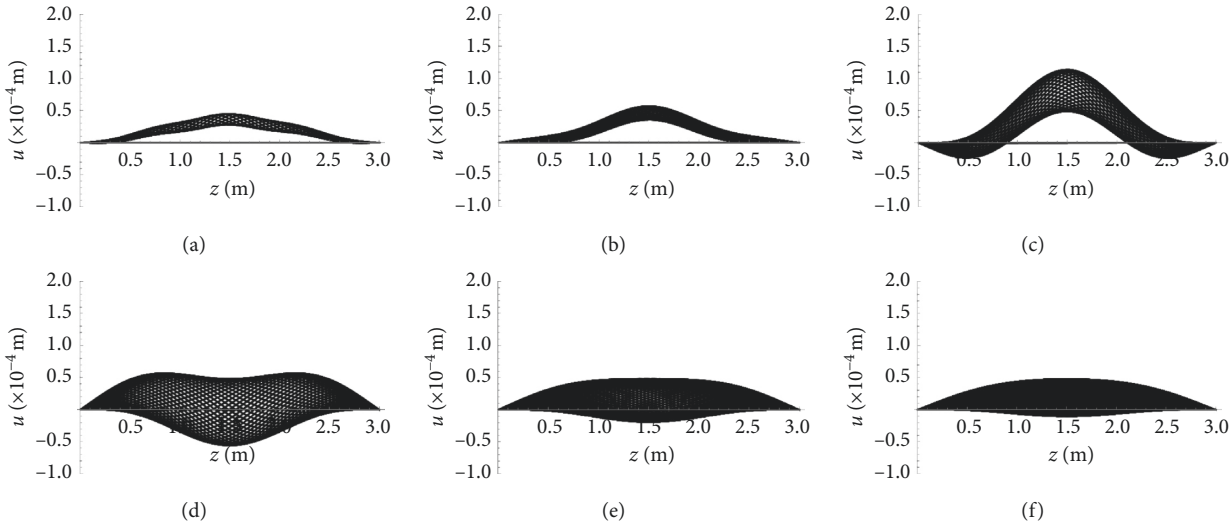

Figure 11: Nondimensional displacement at one of the forcing points during a loading period for different angular speeds for $c = 1.1$. (a) $\omega = 200$ rpm; (b) $\omega = 400$ rpm; (c) $\omega = 600$ rpm; (d) $\omega = 800$ rpm; (e) $\omega = 1000$ rpm; (f) $\omega = 1200$ rpm.

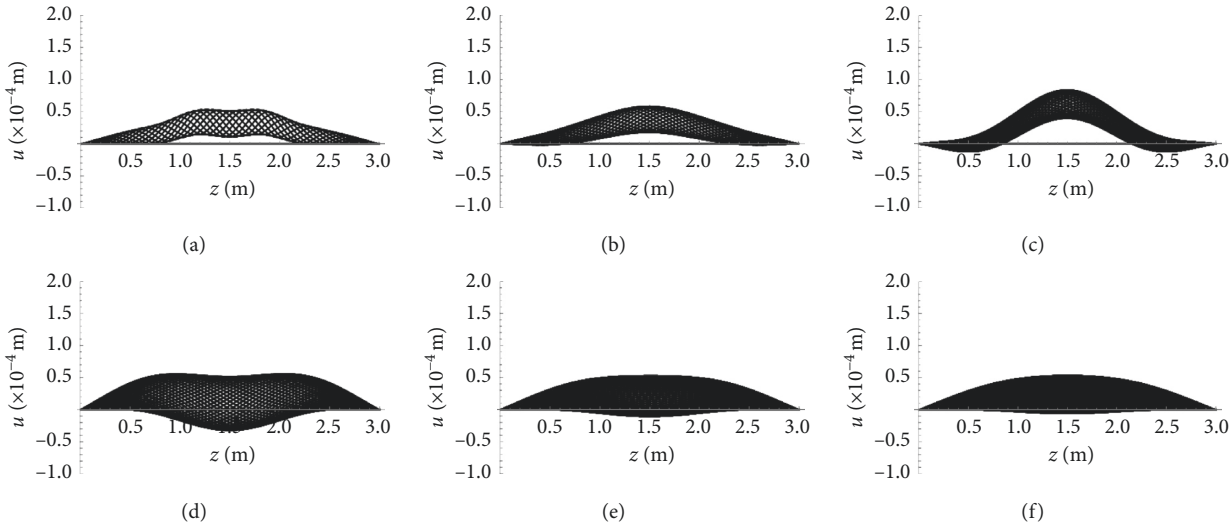

Figure 12: Nondimensional displacement at one of the forcing points during a loading period for different angular speeds for $c = 1.25$. (a) $\omega = 200$ rpm; (b) $\omega = 400$ rpm; (c) $\omega = 600$ rpm; (d) $\omega = 800$ rpm; (e) $\omega = 1000$ rpm; (f) $\omega = 1200$ rpm.

Therefore, this operating condition should be avoided, operating at different speed values or using a shaft damping system or, finally, designing the blades to have a contact ratio greater than 1 (see next section). It is worth noting that, if the machine is conceived to operate at speed values higher than the load-critical speed, its value has to be crossed during machine run up and coast down and particular caution should be adopted in this phase.

2.5.4. Case Study 4. Figures 11 and 12 show the effect of the contact ratio on the shaft deformation for the 4-blade configuration. In particular, Figure 11 shows the shaft deformation for different speed values in the case $c = 1.1$, while Figure 12 is obtained for $c = 1.25$. As the contact ratio increases, that is, two perforation points simultaneously act at the beginning and at the end of the shaft, no appreciable differences, if compared with $c = 1.0$ case, are found far from the load-critical speed values ($\omega = 200$, 400, 800, 1000, 1200 rpm), being the shaft deformation always lower than 0.1 mm. Only a thickening of the response curve envelope is observed related to differences in consecutive runs.

A more in-depth analysis has to be carried out in the proximity of the load-critical speed. Figure 13 shows the shaft deformation for $\omega = 0.98\overline{\omega}$ for the different contact ratio cases. In order to fully represent the shaft deformation, it is worth noting that the plot range is larger than in the previous Figures 6–12.

The curve shape is the same for the three cases, being the shaft deformation negative close to the shaft ends and

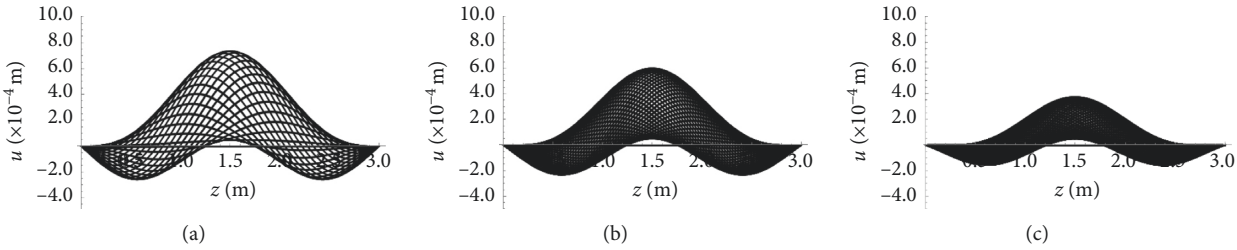

Figure 13: Nondimensional displacement at one of the forcing points during a loading period for different angular speeds for 4-blade configuration. (a) c = 1, (b) c= 1.1, and (c) c=1.25.

positive in the center, causing irregular perforation in real application. However, the amplitude of the shaft deformation is lower as the contact ratio increases, and, consequently, the perforation force will be more uniform along the shaft.

3. Conclusions

An analytical model of a shaft subject to a moving load was developed starting from the literature. Its configuration draws inspiration by paper converting machinery, in particular by the paper roll perforating unit. The model is based on modal superposition, and it is able to provide useful indications to the designer considering just the first natural mode of the shaft because, as demonstrated, the second (and higher) natural mode contribution is negligible from an engineering point of view.

It is shown that with a contact ratio equal to 1, resonance is possible when the forcing point travels along the shaft in a time equal to the shaft natural period, that is, when the frequency of rotation is equal to the shaft flexural eigenfrequency divided by the number of blades. Therefore, among the most influential design parameters on the shaft vibratory behavior, there are the shaft mass and stiffness, which determine its eigenfrequency, and the number of blades, which multiplied by the rotation frequency, that determine the frequency of excitation. On the basis of the operating speed which is fixed depending on the whole paper converting process, the shaft designer can choose suitable parameters to avoid critical conditions.

In addition to those parameters, there is also the contact ratio, which slightly affects the excitation frequency. The simulations show that increasing the contact ratio in most cases flattens the deformed shape, generally leading to a lower vibration level especially close to the resonance frequency.

Therefore, in case of operation near critical speeds, possible corrective actions are those aimed at shifting shaft eigenfrequencies by modifying its stiffness or mass, at shifting excitation frequency by changing the number of blades, and at smoothing the deformed shape by increasing the contact ratio.

Future work will be devoted to include support finite stiffness and countershaft elastic reaction in the model.

Data Availability

The numeric data used to support the findings of this study are available from the corresponding author upon request.

Conflicts of Interest

The authors declare that there are no conflicts of interest regarding the publication of this paper.

Acknowledgments

The authors are grateful to the University of Pisa for supporting this research activity (grant no. PRA_2018_80).

References

[1] H. Ouyang, "Moving-load dynamic problems: a tutorial (with a brief overview)," *Mechanical Systems and Signal Processing*, vol. 25, no. 6, pp. 2039–2060, 2011.

[2] L. Frýba, *Dynamics of Railway Bridges*, Telford, London, UK, 2nd edition, 1996.

[3] R. Katz, C. W. Lee, A. G. Ulsoy, and R. A. Scott, "The dynamic response of a rotating shaft subject to a moving load," *Journal of Sound and Vibration*, vol. 122, no. 1, pp. 131–148, 1988.

[4] H. P. Lee, "Dynamic response of a rotating Timoshenko shaft subject to axial forces and moving loads," *Journal of Sound and Vibration*, vol. 181, no. 1, pp. 169–177, 1995.

[5] A. Argento, "A spinning beam subjected to a moving deflection dependent load,," *Journal of Sound and Vibration*, vol. 182, no. 4, pp. 595–615, 1995.

[6] A. Argento and H. L. Morano, "A spinning beam subjected to a moving deflection dependent load,," *Journal of Sound and Vibration*, vol. 182, no. 4, pp. 617–622, 1995.

[7] Y.-M. Huang and C.-Y. Lee, "Dynamics of a rotating Rayleigh beam subject to a repetitively travelling force," *International Journal of Mechanical Sciences*, vol. 40, no. 8, pp. 779–792, 1998.

[8] H. Ouyang and M. Wang, "A dynamic model for a rotating beam subjected to axially moving forces," *Journal of Sound and Vibration*, vol. 308, no. 3–5, pp. 674–682, 2007.

[9] Y. M. Huang and M. L. Yang, "Dynamic analysis of a rotating beam subjected to repeating axial and transverse forces for simulating a lathing process," *International Journal of Mechanical Sciences*, vol. 51, no. 3, pp. 256–268, 2009.

[10] W. C. Hsu, C. H. Kang, Y. W. Chen, T. N. Shiau, and D. S. Liu, "Dynamic analysis of a rotating shaft subject to the double cutting force and time-varying mass effects of the rod," *Procedia Engineering*, vol. 79, pp. 386–396, 2014.

[11] B. Lv, W. Li, and H. Ouyang, "Moving force-induced vibration of a rotating beam with elastic boundary conditions," *International Journal of Structural Stability and Dynamics*, vol. 15, no. 1, Article ID 1450035, 24 pages, 2015.

[12] G. J. Sheu and S. M. Yang, "Dynamic analysis of a spinning Rayleigh beam," *International Journal of Mechanical Sciences*, vol. 47, no. 2, pp. 157–169, 2005.

[13] A. V. Pesterev, B. Yang, L. A. Bergman, and C. A. Tan, "Revisiting the moving force problem," *Journal of Sound and Vibration*, vol. 261, no. 1, pp. 75–91, 2003.

[14] C. P. S. Kumar, C. Sujatha, and K. Shankar, "Vibration of simply supported beams under a single moving load: a detailed study of cancellation phenomenon," *International Journal of Mechanical Sciences*, vol. 99, pp. 40–47, 2015.

[15] C. Svedholm, A. Zangeneh, C. Pacoste, S. François, and R. Karoumi, "Vibration of damped uniform beams with general end conditions under moving loads," *Engineering Structures*, vol. 126, pp. 40–52, 2016.